

Analysis of diffraction imaging in non-conjugate configurations

Ran Pan,¹ Yuanming Feng,¹ Yu Sa,^{1,2} Jun Q. Lu,³ Kenneth M. Jacobs,³
and Xin-Hua Hu^{3,1,*}

¹Department of Biomedical Engineering, Tianjin University, Tianjin 300072, China

²sayu@tju.edu.cn

³Department of Physics, East Carolina University, Greenville, NC 27858, USA D.C. 20036, USA

*hux@ecu.edu

Abstract: Diffraction imaging of scattered light allows extraction of information on scatterer's morphology. We present a method for accurate simulation of diffraction imaging of single particles by combining rigorous light scattering model with ray-tracing software. The new method has been validated by comparison to measured images of single microspheres. Dependence of fringe patterns on translation of an objective based imager to off-focus positions has been analyzed to clearly understand diffraction imaging with multiple optical elements. The calculated and measured results establish unambiguously that diffraction imaging should be pursued in non-conjugate configurations to ensure accurate sampling of coherent light distribution from the scatterer.

©2014 Optical Society of America

OCIS codes: (110.1650) Coherence imaging, (050.1940) Diffraction.

References and links

1. J. Neukammer, C. Gohlke, A. Hope, T. Wessel, and H. Rinneberg, "Angular distribution of light scattered by single biological cells and oriented particle agglomerates," *Appl. Opt.* **42**, 6388-6397 (2003).
2. K. M. Jacobs, L. V. Yang, J. Ding, A. E. Ekpenyong, R. Castellone, J. Q. Lu, and X. H. Hu, "Diffraction imaging of spheres and melanoma cells with a microscope objective," *J. Biophotonics* **2**, 521-527 (2009).
3. K. M. Jacobs, J. Q. Lu, and X. H. Hu, "Development of a diffraction imaging flow cytometer," *Opt. Lett.* **34**, 2985-2987 (2009).
4. X. Su, S. E. Kirkwood, M. Gupta, L. Marquez-Curtis, Y. Qiu, A. Janowska-Wieczorek, W. Rozmus, and Y. Y. Tsui, "Microscope-based label-free microfluidic cytometry," *Opt. Express* **19**, 387-398 (2010).
5. K. Dong, Y. Feng, K. M. Jacobs, J. Q. Lu, R. S. Brock, L. V. Yang, F. E. Bertrand, M. A. Farwell, and X. H. Hu, "Label-free classification of cultured cells through diffraction imaging," *Biomed. Opt. Express* **2**, 1717-1726 (2011).
6. Y. Sa, J. Zhang, M. S. Moran, J. Q. Lu, Y. Feng, and X. H. Hu, "A novel method of diffraction imaging flow cytometry for sizing microspheres," *Opt. Express* **20**, 22245-22251 (2012).
7. Y. Feng, N. Zhang, K. M. Jacobs, W. Jiang, L. V. Yang, Z. Li, J. Zhang, J. Q. Lu, and X. H. Hu, "Polarization imaging and classification of Jurkat T and Ramos B cells using a flow cytometer," *Cytometry A* **85**, 817-826 (2014).
8. S. Holler, Y. Pan, R. K. Chang, J. R. Bottiger, S. C. Hill, and D. B. Hillis, "Two-dimensional angular optical scattering for the characterization of airborne microparticles," *Opt. Lett.* **23**, 1489-1491 (1998).
9. A. Sommerfeld, *Optics* (Academic Press, 1954), p. 179.
10. J. S. A. Collins, "Lens-system diffraction integral written in terms of matrix optics," *J. Opt. Soc. Am.* **60**, 1168-1177 (1970).
11. P. Török, "Propagation of electromagnetic dipole waves through dielectric interfaces," *Opt. Lett.* **25**, 1463-1465 (2000).
12. B. Lee, S. Min, and B. Javidi, "Theoretical analysis for three-dimensional integral imaging systems with double devices," *Appl. Opt.* **41**, 4856-4865 (2002).
13. M. Speidel, A. Jona, and E. Florin, "Three-dimensional tracking of fluorescent nanoparticles with subnanometer precision by use of off-focus imaging," *Opt. Lett.* **28**, 69-71 (2003).
14. I. R. Capoglu, C. A. White, J. D. Rogers, H. Subramanian, A. Taflove, and V. Backman, "Numerical simulation of partially coherent broadband optical imaging using the finite-difference time-domain method," *Opt. Lett.* **36**, 1596-1598 (2011).
15. C. F. Bohren, and D. R. Huffman, *Absorption and Scattering of Light by Small Particles* (Wiley, 1983), p. 65.
16. K. Kusaka, S. Adachi, and K. Yamazaki, "Microscopic objective having a long working distance," US Patent: 6,069,744 (US Patent Office, 2000).

17. Y. Sa, Y. Feng, K. M. Jacobs, J. Yang, R. Pan, I. Gkigkitzis, J. Q. Lu, and X. H. Hu, "Study of low speed flow cytometry for diffraction imaging with different chamber and nozzle designs," *Cytometry A* **83**, 1027-1033 (2013).
 18. J. Zhang, Y. Feng, M. S. Moran, J. Q. Lu, L. V. Yang, Y. Sa, N. Zhang, L. Dong, and X. H. Hu, "Analysis of cellular objects through diffraction images acquired by flow cytometry," *Opt. Express* **21**, 24819-24828 (2013).
 19. J. Q. Lu, P. Yang, and X. H. Hu, "Simulations of light Scattering from a biconcave red blood cell using the FDTD method," *J. Biomed. Opt.* **10**, 024022 (2005).
-

1. Introduction

Diffraction imaging samples the intensity distribution of coherent light elastically scattered by a particle. For a wavelength sized scatterer, the acquired images present distinct patterns characteristic of its 3D morphology in terms of density distribution of induced dipoles or refractive index. Therefore, analysis of diffraction images could enable morphology based identification and classification of scatterers including biological cells without fluorescence labeling. Diffraction imaging of small scatterers in optical domain has been carried out with an objective which can also be used to align the excitation beam and small scatterers under non-coherent illumination [1-7].

A method of diffraction imaging flow cytometry (DIFC) has been developed with an objective based imager to detect side scatter for rapid characterization of scatterers including biological cells [2, 3, 5-7]. Unexpectedly, we observed that subsequent imaging of the coherent scatter is best achieved by translating the imager to off-focus positions toward the scatterer. Furthermore, diffraction imaging in these non-conjugate configurations has been shown to yield patterns of strong correlation to the scatterer's morphology [2, 3, 5-7] and improved contrast in comparison to previous results [1, 4, 8]. Despite these experimental observations, coherent imaging with numerous optical elements such as the objective has not been clearly understood. It is therefore interesting and very useful to develop tools for study of diffraction imaging with optics designed for non-coherent or diffraction-limited imaging.

Sommerfeld defined diffraction as "any deviation of light rays from rectilinear paths which cannot be interpreted as reflection or refraction" [9]. Maxwell or wave equations, including various scalar-field models such as Fresnel diffraction integral, have been solved for accurate modeling propagation of coherent wavefields [10-14]. Direct application of these vector- or approximate scalar-field methods to objective based imagers is challenging because of large number of lenses involved for image simulation and can lead to significant cumulative errors if an approximate model is adopted. Analysis of diffraction imaging with the existing methods in off-focus or non-conjugate configurations is particularly difficult where a practical imaging system has to be examined in details [12, 13]. In this report we present a method for calculation of diffraction images acquired through optical systems with a rigorous scattering model to obtain light distribution on an input plane in the host medium of the scatterer and ray-tracing software to obtain the light distribution on an image plane. Comparison to images measured with a DIFC system with single microspheres were performed for validation. Diffraction imaging have been analyzed in details with the new method to clearly understand the effect of optical system in non-conjugate configurations.

2. Methods

We first established in the ray-tracing software (Zemax-EE v2009, Zemax Development Corp.) an optical system consisting of host medium of the scatterer, flow chamber and imager or imaging unit as shown in Fig. 1(a). The imager includes an infinity-corrected objective of long working distance (WD) and large numerical aperture (NA), a tube lens of focal length f that defines the image plane at its focus. As shown in Fig. 1(b), a laminar flow of water carries a microsphere along the negative y direction and enters into the focus of an incident laser beam along the z -axis. To understand coherent imaging in non-conjugate configurations as defined in conventional imaging analysis, we direct our attention to the relation of intensity distributions of scattered light between an input plane and the image plane. As illustrated in

Fig. 1(b), the former is defined as a plane in the host medium located 0.15mm from the scatterer's center. The areas of field-of-view (FOV) on the input or image planes are defined by either the actual image sensor or for accommodating all rays allowed by the aperture stop of the objective. The scattered light form a cone in water from the scatterer with θ_{wm} as the maximum cone angle with the exit pupil filled fully. The imager can be translated as a whole along the x-axis with $\Delta x=0$ indicating the configuration in which the position of scatterer as the object is conjugate to the image plane. Cases of $\Delta x > 0$ refer to the non-conjugate configurations by translating the imager off-focus toward the scatterer.

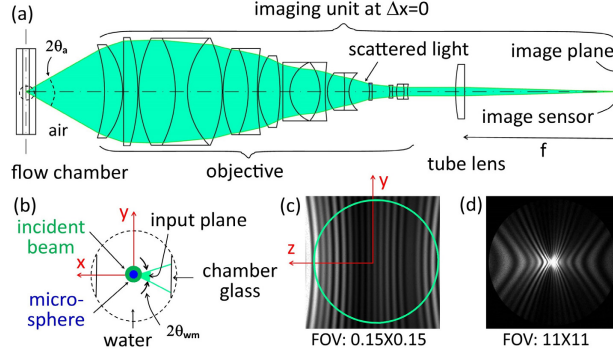


Fig. 1. (a) The schematic of optical system: $NA=\sin\theta_a$ for the objective and green area indicating the cone of imaged rays; (b) the scattering geometry with microsphere at the focus of incident beam along z-axis and θ_{wm} being the cone angle of imaged rays in water; (c) S_{11} projected on input plane with range of imaged rays marked by the green circle; (d) ray-tracing results at image plane with $\Delta x=0$ and other parameters given in Fig. 2. FOV sizes are in the unit of mm^2 .

To account for the coherent nature of scattered light by microspheres, we used the Mie theory in terms of the Mueller matrix elements [15] to obtain the angle-resolved distribution of scattered light intensity. For simplicity, we consider unpolarized imaging here using the Mueller matrix element $S_{11}(\theta_s, \phi_s)$, where θ_s and ϕ_s is respectively the polar and azimuthal angle of scattered light. The present method can be straightforwardly generalized for polarized imaging of coherent light with other Mueller matrix elements [7]. An input data file to Zemax was first created by projecting $S_{11}(\theta_s, \phi_s)$ to the input plane. The values of (θ_s, ϕ_s) and S_{11} determine the initial direction and intensity weight of the rays which are traced through the optical system to obtain light distribution on the image plane. Figs. 1(c) and 1(d) present the light distributions on the two planes for the case of $\Delta x = 0$. One can recognize that the diffraction fringes preserve a unique relation to each other despite “increased bending” of the fringes on the image plane [3]. To compare calculated with the measured images for validation, we employed the simulation parameters as close as possible to those in experiment.

A DIFC prototype instrument (P3, WavMed Technologies Corp.) was used as the experimental system for measurement of diffraction images of microspheres moving at a speed of about 4mm/s. The imaging unit includes an infinity-corrected and non-telecentric 50x objective (378-805-3, Mitutoyo) with nominal values of $NA = 0.55$ and $WD = 13.0$ mm. The design parameters of the objective, however, are proprietary and unavailable for this study. We simulated instead an objective with design parameters given in public domain, which has the same features of infinity-correction, magnification and non-telecentricity but longer WD of 34.8mm than the one in the experimental system [16]. The design was slightly modified to obtain the same value of NA. Other simulation parameters are identical to those of the experimental system [6] with an incident beam of $\lambda = 532$ nm and focused on the core fluid with a diameter of about $20 \mu m$, $d = 9.6 \mu m$ for results presented in Figs. 2 to 5 and refractive index $n_s = 1.588$ for the microsphere, refractive index $n_h = 1.334$ for the host medium of water and $n_g = 1.467$ for the quartz glass of the flow chamber with 3.0mm and 5.5mm for inner and outer side lengths along the x- and z-axis respectively, $f = 75$ mm for the

tube lens. A camera (LM 075M, Lumenera) of 640x480 pixels was used to acquire images with exposure time set at 1 ms.

3. Results and discussion

We measured diffraction images of different microsphere at different Δx . Two types of microspheres of diameter $d = 9.6 \mu\text{m}$ and $5.7 \mu\text{m}$ were used for measurement and similar changes in fringe patterns were observed among images acquired at different positions of Δx . Fig. 2 presents examples the diffraction images acquired with the microspheres of $d = 9.6 \mu\text{m}$ and the imager translated from $\Delta x = 450$ to $-450 \mu\text{m}$ with the core fluid speed kept low at about 4mm/s to reduce blurring [17]. It can be seen from these results that the diffraction images acquired with $\Delta x > 0$ presents much higher similarity in fringe patterns to the one on the input plane as shown in Fig. 1(c) than those acquired with $\Delta x < 0$.

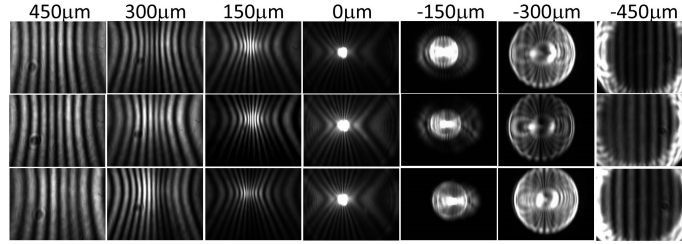


Fig. 2. Measured diffraction images of single polystyrene microspheres of $d=9.6\mu\text{m}$ acquired with the imaging unit translated to Δx as marked above each column and incident beam of wavelength $\lambda=532\text{nm}$.

For comparison to the measured data in Fig. 2, we set the FOV of the image plane for simulations by including in the calculated image at $\Delta x=150 \mu\text{m}$ the same number of fringes as that of the measured image. Fig. 3 present the calculated images obtained with the imager translated to different positions of Δx marked at the top of the images. All images were normalized for comparison of diffraction patterns. To examine the chamber's effect on imaging, it was replaced by air in calculating images shown on the bottom row of Fig. 3(a). In these cases, the off-focus positions for calculated images refer to an updated focused position of $\Delta x = 0$, which differs from the case with chamber by 1.48mm toward the scatterer.

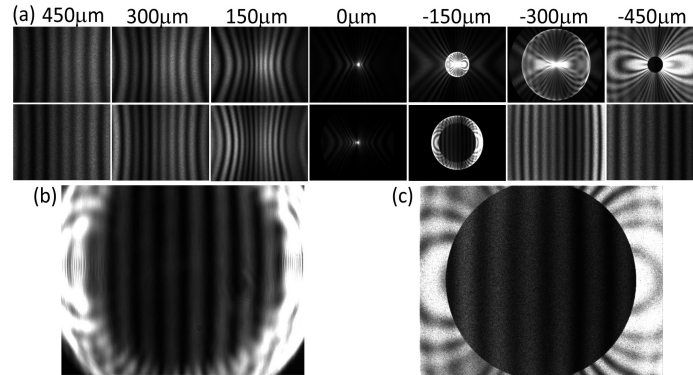


Fig. 3. (a) Calculated diffraction images of microsphere with $d=9.6\mu\text{m}$ obtained at Δx as marked above each column; top row: calculated with flow chamber; bottom row: without flow chamber; (b) the measured and (c) re-calculated images with chamber and reduced cone angle at $\Delta x = -450\mu\text{m}$. The FOV on image plane was set to $3.2 \times 2.4 \text{mm}^2$ in simulations..

Comparison of the measured images in Fig. 2 and the calculated ones in the top row of Fig. 3(a) with different Δx demonstrates good agreement on the dependence of the fringe patterns on Δx . These results thus validate the method presented here for forward calculation of diffraction images at the image plane from the input plane. One notable disagreement

between the measured and calculated images can be seen in the case of $\Delta x = -450 \mu\text{m}$. A close examination of the calculated results showed that disagreement is due to the different cone angles for imaging scattered light between the experimental DIFC system and simulations because of markedly different WD values. Once the cone angle of scattered light on the input plane was reduced in simulation from the exit pupil filling value of $\theta_{wm} = 24.59^\circ$ to 22.05° , the disagreement becomes much less pronounced as shown in Figs. 3(b) and 3(c). This indicates clearly that variation of θ_{wm} in cases of negative Δx can alter the fringe patterns quite drastically. Taking together, the data in Figs. 2 and 3 demonstrate the validity and robustness of the method for accurate simulation of diffraction images.

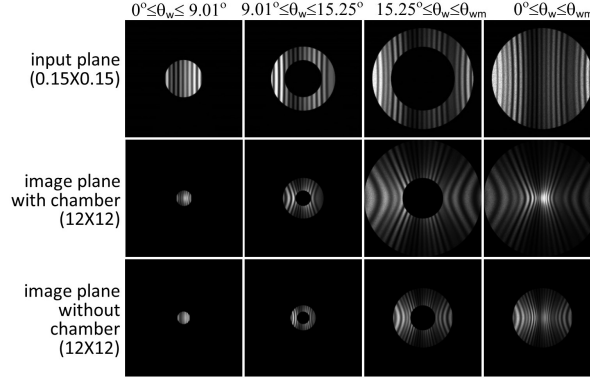


Fig. 4. Calculated images on the input and image planes with $\Delta x=150\mu\text{m}$ in different zones of θ_w with ($\theta_{wm}=23.27^\circ$) and without ($\theta_{wm}=24.45^\circ$) flow chamber. The FOV sizes in parentheses are in the unit of mm^2 .

Images in Figs. 2 and 3 exhibit distinct variations of pattern along the two directions of off-focus translation. At positions of $\Delta x > 0$, the light distributions on the image plane present patterns of unique correspondence to those on the input plane as shown in Fig. 1(c). The existence of the unique mapping relation in these non-conjugate configurations is in stark contrast to the expectation of image blurring in non-coherent imaging. To examine the relation further, we divided the projected image of S_{11} on the input plane into three zones according to θ_w in water and traced scattered light in different zones to obtain corresponding images. Fig. 4 presents the calculated images at the input and image planes of $\Delta x > 0$ with and without the flow chamber. The angle-resolved data in Fig. 4 show unambiguously that a one-to-one relation exists between the fringes on the input and image planes. The non-mixing nature remains the same with or without the flow chamber. Therefore, the flow chamber as an optical element merely reshapes the patterns at off-focus positions of $\Delta x > 0$. Consequently, acquisition of diffraction images for analysis of a scatterer's morphology should be pursued by off-focus imaging with $\Delta x > 0$. In these cases, uniformity and magnification on the image plane are enhanced that benefit subsequent image analysis [5-7, 18].

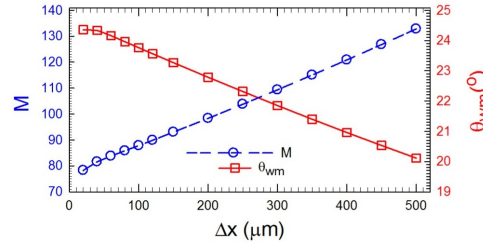


Fig. 5. Image magnification M and maximum cone angle θ_{wm} versus the off-focus position Δx . Other simulation parameters are identical to those in Fig. 2 with the flow chamber. The lines are for visual guide.

While the imaging unit increases the angular range of scattered light falling on the front surface as it moves towards the scatterer, it can be shown with the current method that the maximum cone angle θ_{wm} of scattered light passing through the exit pupil of the objective actually decreases. The changes can be quantified with an image magnification M defined as the diameter ratio of outermost rays on the input and image planes under the condition that the exit pupil is fully filled and the imager positioned at $\Delta x > 0$. In Fig. 5 we plot M and θ_{wm} against Δx and the variations of θ_{wm} and M can be attributed to the non-telecentricity of the imaging optics. Data in Fig. 5 also yield insight on imaging optimization. Translation of the imager toward the scatterer enables magnified views of the diffraction patterns and enhanced uniformness of pixel intensity at the cost of reduced angular range for detection of scattered light. Since the angular range can affect the ability of diffraction imaging to resolve morphological details, one has to balance these considerations with an appropriate Δx .

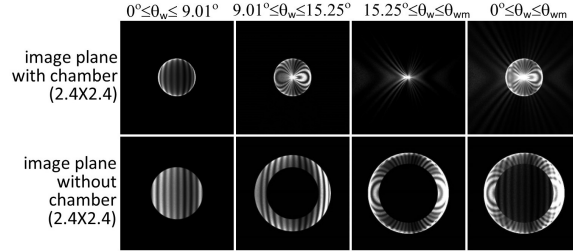


Fig. 6. Calculated images with $\Delta x = -150 \mu\text{m}$ in different zones of θ_w on the image planes with ($\theta_{wm} = 24.44^\circ$) and without ($\theta_{wm} = 24.60^\circ$) flow chamber. The FOV sizes in parentheses are in the unit of mm^2 . The images on the input plane and other simulation parameters are identical to those in Fig. 4.

The significance of the difference between coherent and non-coherent imaging for different non-conjugate configurations may be better grasped with angle-resolved simulations performed with $\Delta x < 0$, as shown in Fig. 6. It can be seen there that all imaged rays from three angular zones on the input plane arrive in the center zone with the flow chamber, thereby leading to image blur on the image plane. Without the chamber, the center zone is cleared of blur which occurs instead in the peripheral ring zone of the image plane. The same shifting of the blur from the center to the peripheral zone occurs with the chamber as well if the imager is translated to far off-focused positions, e.g., $\Delta x = -450 \mu\text{m}$, as evidenced by the calculated images in Fig. 3(a). Obviously, both of the imager and flow chamber as optical elements can affect significantly the patterns presented on the image plane for cases of $\Delta x < 0$. One may conclude from these results that off-focus imaging with $\Delta x < 0$ leads to pattern variations on image plane due to the optical system instead of just the scatterer's morphology, which agree with the previous [2] and current measured data in Fig. 2.

4. Summary

We have developed a robust method for analysis of diffraction imaging through an optical system including objective. The new method consists of a rigorous model of light scattering to obtain accurately the coherent wavefields in far-field and ray-tracing software to calculate subsequent propagating through the system and detected images. The simulation results agree well with measured images and yield significant insight on optimization for diffraction imaging of single scatterers in non-conjugate configurations with $\Delta x > 0$. The current method can be generalized for analysis of polarized diffraction imaging of single biological cells with rigorous numerical models of light scattering through the Mueller matrix [7, 19].

Acknowledgments

X.H. Hu acknowledges support by the Tianjin Science and Technology Commission and Y. Feng acknowledges support by the NSFC (grants 81171342 and 81201148).